

1  
2  
3  
4  
5  
6  
7  
8  
9  
10  
11  
12  
13  
14  
15  
16  
17  
18  
19  
20  
21  
22  
23  
24  
25  
26  
27  
28  
29  
30  
31  
32  
33  
34  
35  
36  
37  
38  
39

*[Journal of Geophysical Research: Solid Earth]*

Supporting Information for

**[Experimental Investigation on the Transport of Sulfide Driven by Melt-rock Reaction in Partially Molten Peridotite]**

[Zhenjiang Wang<sup>1,3</sup>, Zhuo-sen Yao<sup>2</sup>, Zhenmin Jin<sup>3</sup>, Yannan Wang<sup>1</sup>]

<sup>1</sup>Key Laboratory of Resource Exploration Research of Hebei Province, and School of Earth Science and Engineering, Hebei University of Engineering, 056038 Handan, China.

<sup>2</sup>State Key Laboratory of Geological Processes and Mineral Resources, and School of Earth Resources, China University of Geosciences, 430074 Wuhan, China.

<sup>3</sup>State Key Laboratory of Geological Processes and Mineral Resources, and School of Earth Sciences, China University of Geosciences, 430074 Wuhan, China.

Corresponding author: Zhuo-sen Yao and Zhenmin Jin (yaozhuosen@cug.edu.cn; zmjin@cug.edu.cn)]

**Contents of this file**

Text S1 to S2  
Figures S1 to S9  
Tables S1 to S6

**Additional Supporting Information (Files uploaded separately)**

Tables S1. The statistical results of grain sizes of olivine and clinopyroxene in the upper partially molten peridotite of run PC520, PC528, and PC545.  
Tables S2. The statistical results of grain size of sulfide droplets in these experiments of this study.  
Tables S3. The composition of starting materials.  
Tables S4. EPMA data of olivine, Cpx, and Opx for Figures 6-7.  
Tables S5. EPMA data of silicate melt and sulfides for Figure 8.  
Tables S6. The results of the thermodynamically-constrained model for Figures 6-8.

40 **Text S1.** The methodology for the measurement of grain sizes of olivine and clinopyroxene  
41 In this study, grain sizes of olivine and clinopyroxene in the partially molten peridotite were  
42 measured by mapping analyses of electron backscattered diffraction (EBSD) using a Quanta 450  
43 FE-SEM equipped with an HKL Nordlys EBSD detector at the State Key Laboratory of  
44 Geological Processes and Mineral Resources (GPMR) of China University of Geosciences.  
45 Measurements were performed under the conditions of an accelerating voltage of ~ 20 kV, ~ 0.8  
46 μm step size, a beam current of ~ 6 nA, a tilt angle of ~ 70°, and about ~ 20-25 mm working  
47 distance. The smallest detectable grain size was about ~ 4 μm. EBSD patterns of different crystal  
48 minerals are determined by the orientations of the grains being examined. By scanning the beam  
49 in a grid pattern, a map of the grain orientations can be produced. When a discontinuous change  
50 in the orientation occurs, this indicates that a grain boundary has been crossed. The  
51 misorientations of greater than 15° were recorded as being distinct grains. Then, orientation maps  
52 of different crystal minerals can be built using the commercially available software channel5<sup>®</sup> to  
53 obtain grain sizes of different minerals.

54 **Text S2.** The methodology for the measurement of water content in silicate melt using Fourier  
55 transform infrared spectroscopy (FTIR)

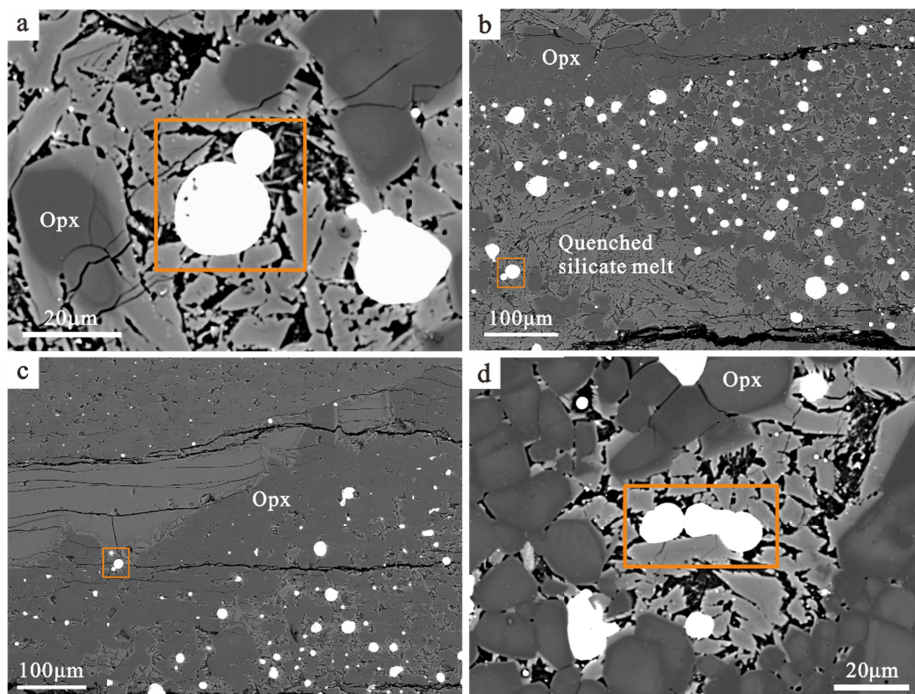
56 We used the FTIR to determine the water content of silicate melt in experiments PC520 and  
57 PC528 at the State Key Laboratory of Geological Processes and Mineral Resources (GPMR) of  
58 China University of Geosciences. Before the FTIR measurements, the samples were double  
59 polished to a thickness of 100 μm and kept in a vacuum stove at 400 K for at least 12h to  
60 preclude the grain boundary water in samples. The water content can be calculated by using the  
61 Beer-Lambert law:

$$62 \quad C_H = \frac{A \times 18.0152}{d \times \rho \times \varepsilon}, \quad (1)$$

63 where  $C_H$  is the total H<sub>2</sub>O content (wt.%),  $A$  is the measured absorbance of the peak at 3550 cm<sup>-1</sup>,  
64 after linear baseline correction ( $\leq 1$ ),  $d$  is the sample thickness (cm);  $\rho$  is the density (g L<sup>-1</sup>) of  
65 silicate melt,  $\varepsilon$  is the molar absorptivity ( $62.8 \pm 0.8$  L mol<sup>-1</sup> cm<sup>-1</sup>) (Mercier et al., 2010).

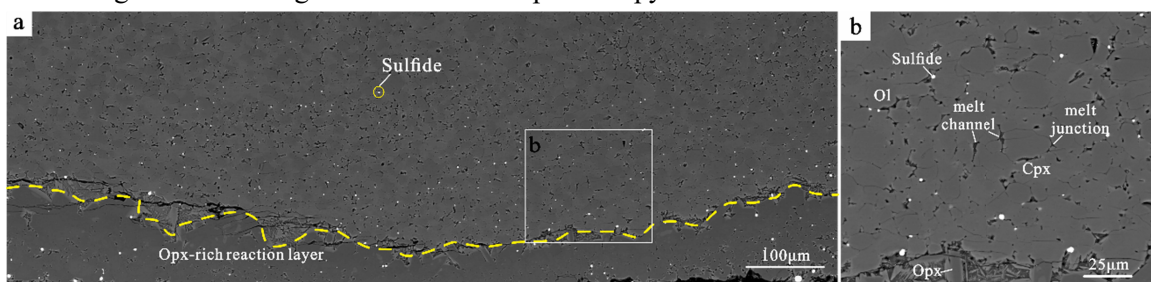
66  
67  
68  
69  
70  
71  
72  
73  
74

76  
77  
78



79

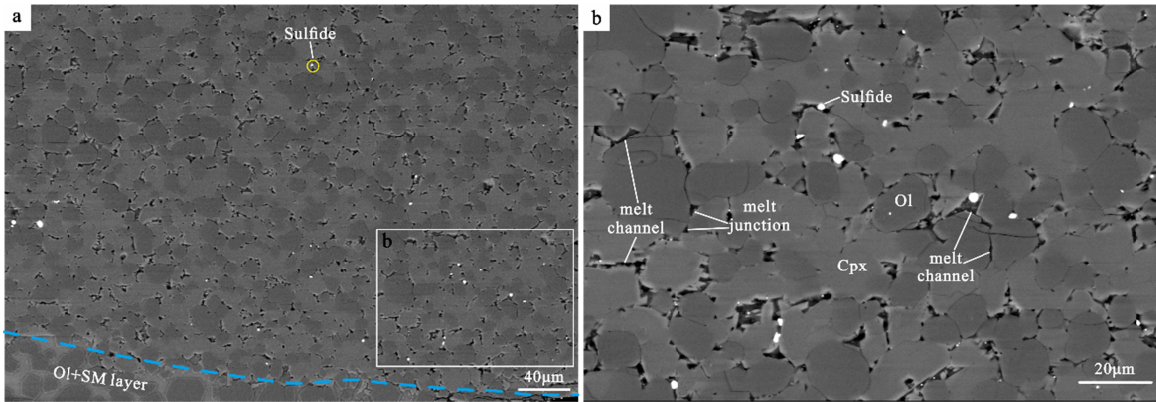
82 **Figure S1.** Microstructures of two sulfide droplets contacting each other from experiments  
83 PC527 (a-b), PC528 (c), and PC545 (d). Yellow squares denote that two sulfide droplets are  
84 contacting and coalescing with each other. Opx-orthopyroxene.



83

88 **Figure S2.** Microstructures of the peridotite and the Opx-rich reaction layer from experiment  
89 PC520 (~ 1.5 GPa, ~ 1,250 °C, ~ 12h). The dashed yellow line denotes the top of the Opx-rich  
90 reaction layer. The bright white spots in the peridotite are sulfide droplets entrained by the  
91 reactive melt flow from the lower melt source. Melt junctions and channels are also designated in  
92 (b). Ol-olivine; Opx-orthopyroxene; Cpx-clinopyroxene.

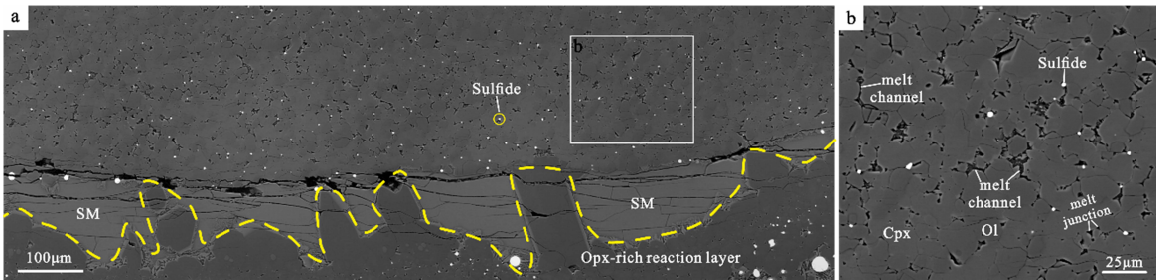
89



90

94 **Figure S3.** Microstructures of the peridotite and the olivine-melt layer (the Ol+SM layer) from  
 95 experiment PC527 (~ 1.5 GPa, ~ 1,300 °C, ~ 12h). The dashed cyan line denotes the top of the  
 96 olivine-melt layer. Symbols are the same as in Figure S2. Ol-olivine; Cpx-clinopyroxene; SM-  
 97 silicate melt.

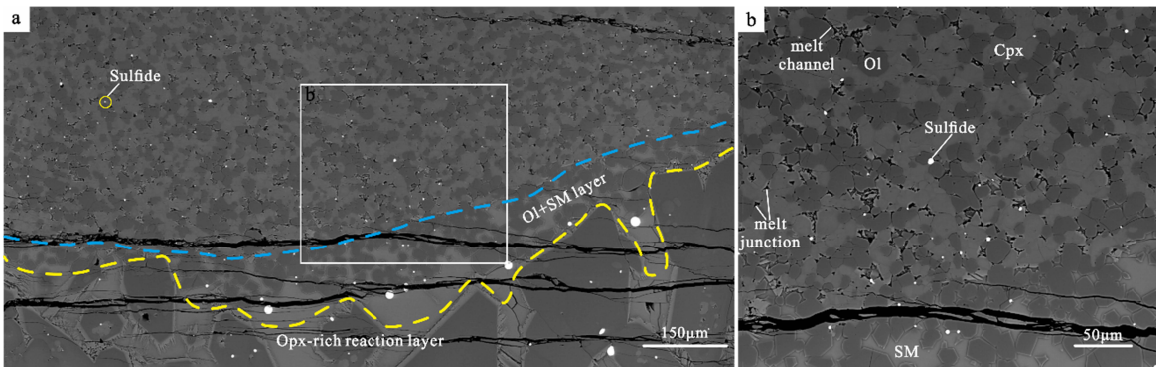
95



96

99 **Figure S4.** Microstructures of the peridotite and the Opx-rich reaction layer from experiment  
 100 PC528 (~ 1.5 GPa, ~ 1,250 °C, ~ 48h). Symbols are the same as in Figure S2. Ol-olivine; Cpx-  
 101 clinopyroxene; Opx-orthopyroxene; SM-silicate melt.

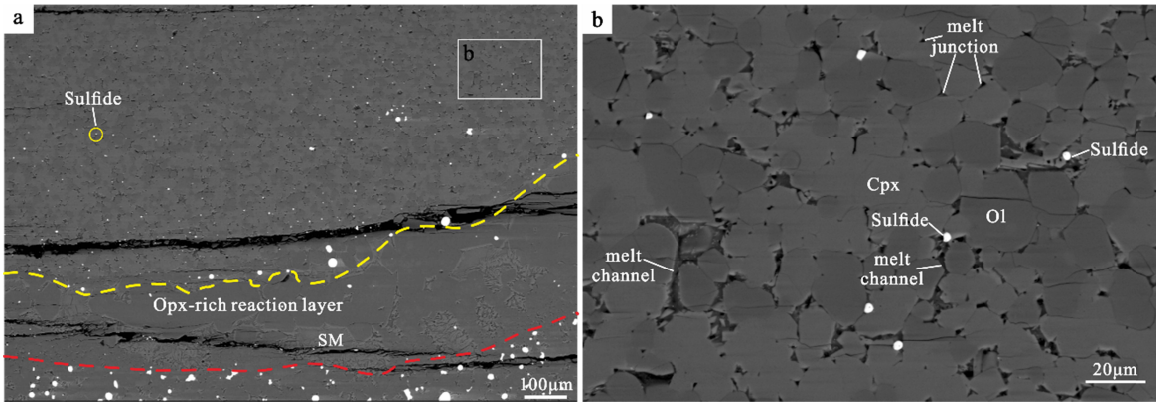
100



101

105 **Figure S5.** Microstructures of the peridotite, the olivine-melt layer, and the Opx-rich reaction  
 106 layer from experiment PC545 (~ 1.5 GPa, ~ 1,250 °C, ~ 72h). The dashed blue and yellow lines  
 107 denote the tops of the olivine-melt layer and Opx-rich reaction layer, respectively. Symbols are  
 108 the same as in Figure S2. Ol-olivine; Opx-orthopyroxene; Cpx-clinopyroxene; SM-silicate melt.

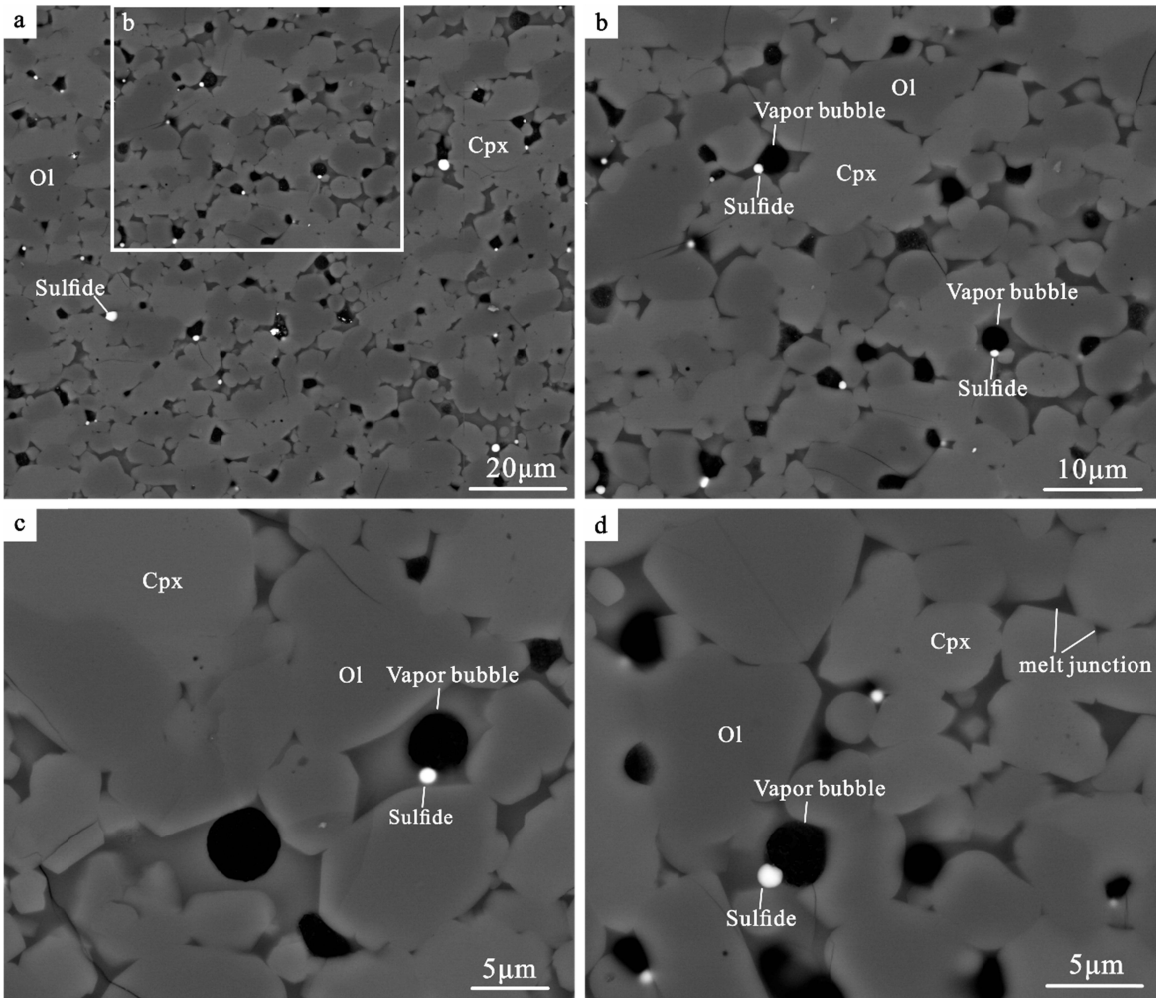
106



107

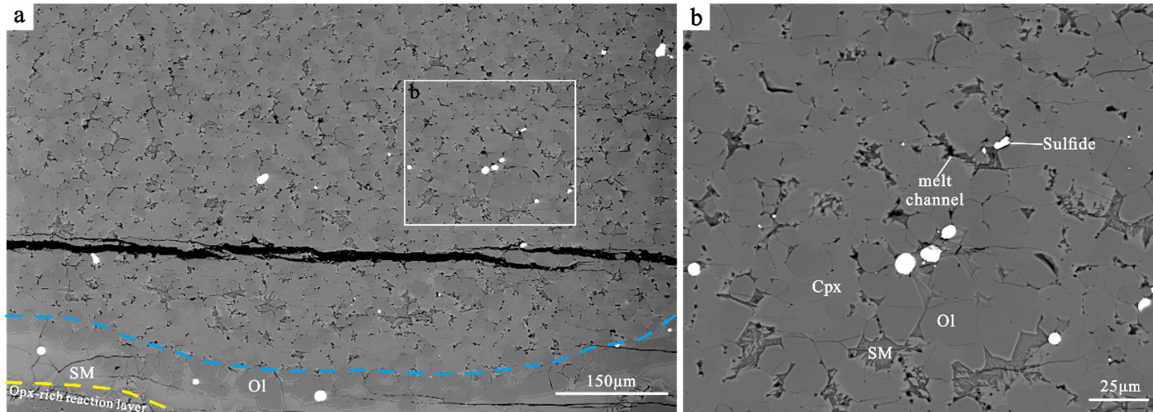
112 **Figure S6.** Microstructures of the peridotite and the Opx-rich reaction layer from experiment  
 113 PC548 (~ 1.5 GPa, ~ 1,250 °C, ~ 48h). The dashed yellow and red lines denote the top of the  
 114 Opx-rich reaction layer and the original interface between the melt source and peridotite before  
 115 the melt-rock reaction, respectively. Symbols are the same as in Figure S2. OI-olivine; Opx-  
 116 orthopyroxene; Cpx-clinopyroxene; SM-silicate melt.

113



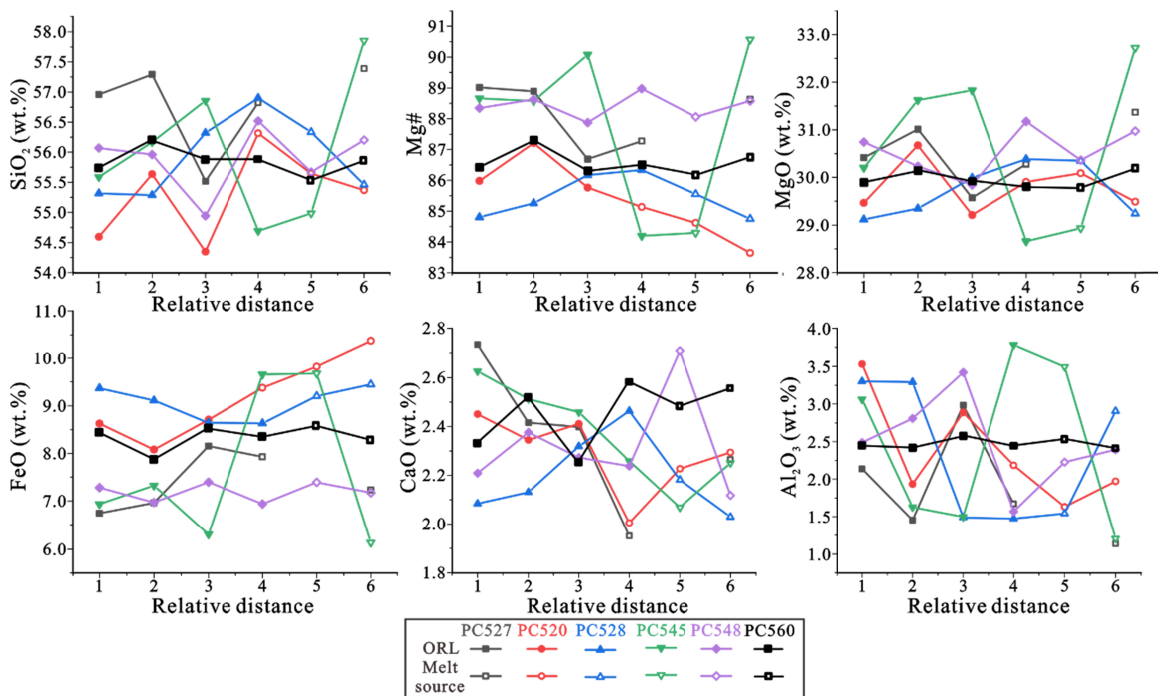
114

118 **Figure S7.** Microstructures of the partially molten peridotite from experiment PC559 (~ 0.5 GPa,  
 119 ~ 1,200 °C, ~ 6h). The low pressure (~ 0.5 GPa) potentially leads to the presence of vapor  
 120 bubbles (mainly H<sub>2</sub>O) in the peridotite, forming some sulfide-vapor aggregates. Symbols are the same as in Figure S2. Ol-olivine; Cpx-clinopyroxene.  
 121  
 119



120

123 **Figure S8.** Microstructures of the peridotite, the olivine-melt layer, and the Opx-rich reaction  
 124 layer from experiment PC560 (~ 1.5 GPa, ~ 1,250 °C, ~ 24h). Symbols are the same as in Figure  
 125 S5. Ol-olivine; Opx-orthopyroxene; Cpx-clinopyroxene; SM-silicate melt.  
 124



125

- 125 **Figure S9.** Plots of analyzed oxide abundance (in wt.%) and Mg# of orthopyroxene grains from  
126 the ORL to the melt source. The relative distance “1” represents the top of the ORL. The  
127 analyzed points are about 50-150  $\mu\text{m}$  apart, depending on the size of orthopyroxene grains and  
128 the thickness of ORL.
- 129 **Table S1.** The statistical results of grain sizes of olivine and clinopyroxene in the upper partially  
130 molten peridotite of run PC520, PC528, and PC545.
- 131 **Table S2.** The statistical results of grain size of sulfide droplets in these experiments of this  
132 study.
- 133 **Table S3.** The composition of starting materials.
- 134 **Table S4.** EPMA data of olivine, Cpx, and Opx for Figures 6-7.
- 135 **Table S5.** EPMA data of silicate melt and sulfides for Figure 8.
- 136 **Table S6.** The results of the thermodynamically-constrained model for Figures 6-8.